

Robust Affine Formation Control of Multiagent Systems

Zhonggang Li, *Student Member, IEEE*, and Raj Thilak Rajan, *Senior Member, IEEE*

Abstract—Affine formation control is a subset of formation control methods, which has gained increasing popularity for its flexibility and maneuverability in diverse applications. Affine formation control is inherently distributed in nature, where the local controllers onboard each agent are linearly dependent on the relative position measurements of the neighboring agents. The unavailability of these measurements in practice, due to node failure or missing links, leads to a change in the underlying graph topology, and subsequently causes instability and sub-optimal performance. In this paper, we propose an estimation framework to enhance the robustness of distributed affine formation control systems against these topology changes. Our estimation framework features an adaptive fusion of both temporal information from the dynamics of agents and spatial information which is derived from the geometry of the affine formations. We propose a suite of algorithms under this framework to tackle various practical scenarios, and numerically verify our proposed estimator on stability, convergence rate, and optimality criterion. Simulations show the performance of our proposed algorithms as compared to the state-of-the-art methods, and we summarize them with future research directions.

Index Terms—distributed filtering, affine formation control, Kalman filtering, relative localization, time-varying graphs.

I. INTRODUCTION

MULTIAGENT systems have been widely researched for their broad applications in various fields such as artificial intelligence [2], swarm robotics [3], social networks [4], and space applications [5]. Various swarm applications require agents to collectively preserve a geometric pattern, i.e., a formation such as collective object transport [6], space-based interferometry [7], or various sensing missions [8]. It relies on measurements of relative information among agents to achieve different formations. For instance, distance measurements are used to achieve rigid formations that allow translations and rotations [9], [10], bearing measurements allow formations with scaling of the geometry [11], [12], and displacements can be employed to realize affine formations [13].

Affine formation control is a subset of general formation control, where the positions of the agents are restricted to affine transformations over time, which include, but are not limited to rotation, translation, and shearing. Since their introduction in 2016 [13], affine formation control has evolved in various directions and has been put into practice [14]. For instance, an extension is made in [15] from shape control to a maneuver control scenario which means the agents are

expected to track a time-varying target configuration with a continuously changing geometry. The underlying graph is also extended to a directed topology [16], [17]. The modeling of agents is generalized from single- and double-integrator agents to more general agents in [18]. The maneuverability of affine formations is achieved by setting a small subset of agents as leaders, whose positions are known. In using a hierarchical control approach for the leaders [19], special cases of affine transformation can be realized. Recent works also show that some maneuvers can be achieved by modifying the stress matrix [20], [21] without the need for leaders. Apart from the controller designs, distributed filtering is also developed and applied to yield more optimal implementations in noisy environments [22]. In general, affine formation control has a relatively simple controller design, but its stability relies on the rigidity of the underlying framework which can be demanding in practice.

Distributed Affine formation control, inherently relies on relative position information of neighborhood nodes, which needs to be measured and communicated. Any failure of the sensing or the communication in practice will change the underlying graph topology, which may cause stability and optimality issues. In networked and distributed control literature, this problem can be modeled as either a switching topology or packet dropouts. For switching topology, state-of-the-art solutions often model the possible topologies and predevelop stabilizing controllers for each [23], [24], [25]. This approach usually implies that the system is stabilizable under each topology such that a controller can be designed among other practical considerations. However, this condition is too restrictive for affine formation control due to the rigidity requirements [13]. Also, switching topology typically does not deal with scenarios where the departures of agents do not affect the formation of the others. On the other hand, packet dropouts, which model an intermittent behavior for the observations [26], [27], can be addressed by estimating the missing information on a fixed topology. This type of method relies on estimator designs but can simplify the problem on the control end. If the estimation is sufficiently accurate, the system exhibits the same closed-loop stability and optimality. For instance, [28] employed long short-term memory to predict the position of the leaders in the event of packet losses. Other common approaches include Kalman filtering to predict the missing information based on the dynamic models [29]. However, these methods are not designed for permanent information loss, e.g., a departing node. In general, there lacks a unified approach to tackle all potential topological changes for affine formation control.

The authors are with Signal Processing Systems, Faculty of Electrical Engineering, Mathematics and Computer Science (EEMCS), Delft University of Technology, Delft, The Netherlands. {z.li-22, r.t.rajan@tudelft.nl}. A part of this work is published in [1] at the 26th International Conference on Information Fusion 2023.

A. Contributions

In this work, we propose a generic distributed estimation framework in discrete time for robust affine formation control. We model the topology changes as the observation losses or edge unavailability, which are then estimated using our proposed observation model. We propose a fusion of temporal and spatial information in the framework, which enable a wide range of practical scenarios to be tackled, including random and permanent observation losses and node departures. Our main contributions are as follows.

- We propose an observation model of relative positions that accounts for the noises introduced in the measurements and their unavailabilities.
- We adopt the Kalman filters in a relative state-space model to address intermittent losses, which is named relative Kalman filtering (RKF). We also propose an estimator using the geometry of affine formations, which we call relative affine localization (RAL), and also propose an improved variant that adopts a dynamic consensus i.e., consensus RAL (conRAL). Our proposed framework that fuses RKF and RAL is called geometry-aware Kalman filtering (GA-RKF).
- In our fusion framework, we propose a key adaptive indicator that locally approximates the system convergence, and show this adaptive indicator is mathematically bounded by the tracking error, the common global convergence indicator.

Layout: In Section II, the preliminaries of affine formation control are introduced and the representation of topology changes is modeled as a time-varying functional graph. In Section III, we motivate the need to model partial observations and give the observation model in a state-space form. In Section IV, we discuss the geometry estimator design in detail and options for improvements. The local convergence indicator, which plays a critical role in adaptive fusion is introduced in Section V followed by some algorithms designs under the proposed framework in Section VI. Numerical validations to test our proposed algorithms are performed in Section VII and followed by conclusions and future works.

Notation: Vectors and matrices are represented by lowercase and uppercase boldface letters respectively such as \mathbf{a} and \mathbf{A} . The elements of matrix \mathbf{A} are expressed using $[\mathbf{A}]_{ij}$ where i and j denote the index of rows and columns, respectively. Sets and graphs are represented using calligraphic letters e.g., \mathcal{A} , and the intersection and union of sets are \cap and \cup , respectively. The relative complement of two sets is denoted by \setminus . Vectors of length N of all ones and zeros are denoted by $\mathbf{1}_N$ and $\mathbf{0}_N$, respectively. An identity matrix of size N is denoted by \mathbf{I}_N . The Kronecker product is \otimes and a vectorization of a matrix is denoted by $\text{vec}(\cdot)$ by stacking all the columns vertically. The trace operator is denoted by $\text{tr}(\cdot)$. We also use subscripts k on vectors and matrices to indicate a time-varying variable.

II. PRELIMINARIES

A. Graph Theory

We consider a setup where N mobile agents work in D -dimensional space with D typically being 2 or 3. The

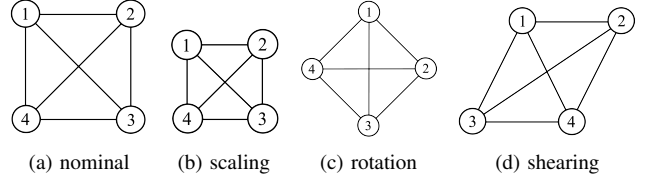


Fig. 1: Illustration of some basic geometric transformations.

$$\mathbf{B} = \begin{bmatrix} 1 & 1 & 1 & -1 & 0 & 0 & -1 & 0 & 0 & -1 & 0 & 0 & -1 & 0 & 0 \\ -1 & 0 & 0 & 1 & 1 & 1 & 0 & -1 & 0 & 0 & -1 & 0 & 0 & -1 & 0 \\ 0 & -1 & 0 & 0 & -1 & 0 & 1 & 1 & 1 & 0 & 0 & -1 & 0 & 0 & -1 \\ 0 & 0 & -1 & 0 & 0 & -1 & 0 & 0 & -1 & 1 & 1 & 1 & 1 & 1 & 1 \end{bmatrix}$$

$\mathbf{B}_1 \qquad \mathbf{B}_2 \qquad \mathbf{B}_3 \qquad \mathbf{B}_4$

Fig. 2: The bidirectional incidence matrix of the nominal graph shown in Fig. 1(a)

underlying connections of the agents are described by an undirected *nominal graph* $\mathcal{G} = (\mathcal{V}, \mathcal{E})$ where the set of vertices is $\mathcal{V} = \{1, \dots, N\}$ and the set of edges is $\mathcal{E} \subseteq \mathcal{V} \times \mathcal{V}$. As an undirected graph is equivalent to a bidirectional graph, i.e., $(i, j) \in \mathcal{E} \Leftrightarrow (j, i) \in \mathcal{E}$, we assume there are M directed edges (or $M/2$ undirected edges) in total. The set of neighbors of a node i is defined as $\mathcal{N}_i = \{j \in \mathcal{V} : (i, j) \in \mathcal{E}\}$, and the corresponding cardinality is denoted by N_i with $\sum_{i \in \mathcal{V}} N_i = M$. The time-varying *functional graph* that represents the actual connectivity of the system is $\mathcal{G}_k = (\mathcal{V}_k, \mathcal{E}_k)$ where k is the discrete-time subscript. It is a subgraph of the nominal graph where the vertex set and the edge set are both subsets of those in the nominal graph, i.e., $\mathcal{V}_k \subseteq \mathcal{V}$ and $\mathcal{E}_k \subseteq \mathcal{E}$. As such, there are $N_k \leq N$ nodes in the functional graph. Similarly, the time-varying cardinality of the set of neighbors is denoted by $N_{i,k}$ with $N_{i,k} \leq N_i$.

In this work, we frequently use the *incidence matrix* of a graph. For the functional graph, the bidirectional incidence matrix $\mathbf{B}_k \in \mathbb{R}^{N \times M_k}$ is defined by

$$[\mathbf{B}_k]_{ij} = \begin{cases} 1 & \text{if edge } e_j \in \mathcal{E}_k \text{ leaves node } i \\ -1 & \text{if edge } e_j \in \mathcal{E}_k \text{ enters node } i \\ 0 & \text{otherwise} \end{cases}, \quad (1)$$

which admits the structure $\mathbf{B}_k = [\mathbf{B}_{1,k}, \mathbf{B}_{2,k}, \dots, \mathbf{B}_{N,k}]$ where the matrix $\mathbf{B}_{i,k} \in \mathbb{R}^{N \times N_i}$, $\forall i \in \mathcal{V}$, group the columns per agent. As an example, the incidence matrix \mathbf{B} of the nominal graph shown in Fig. 1 can be found in Fig. 2, and the time-varying \mathbf{B}_k for the functional graph collects a subset of the columns from each block based on edge availability.

B. Geometric Transformations

We define $\mathbf{z}_{i,k} \in \mathbb{R}^D$ as the time-varying position of agent i at time instant k , and collect all the positions of the agents in a *configuration matrix* $\mathbf{Z}_k = [\mathbf{z}_{1,k}, \mathbf{z}_{2,k}, \dots, \mathbf{z}_{N,k}] \in \mathbb{R}^{D \times N}$. Similarly, a *target configuration* that collects the expected positions of agents is defined as $\mathbf{Z}_k^* = [\mathbf{z}_{1,k}^*, \mathbf{z}_{2,k}^*, \dots, \mathbf{z}_{N,k}^*]$ in which $\mathbf{z}_{i,k}^*$ is the individual target position for each agent $i \in \mathcal{V}$. For the nominal graph \mathcal{G} , we introduce a *nominal configuration* $\mathbf{P} = [\mathbf{p}_1, \mathbf{p}_2, \dots, \mathbf{p}_N]$ where \mathbf{p}_i is the nominal

TABLE I: Key notations for configurations

config.	notation ($\mathbb{R}^{D \times N}$)	local rep. (\mathbb{R}^D)	description
nominal	\mathbf{P}	\mathbf{p}_i	fixed, s.t. design
target	\mathbf{Z}_k^*	$\mathbf{z}_{i,k}^*$	mapped by (2)
real-time	\mathbf{Z}_k	$\mathbf{z}_{i,k}$	s.t. control

position for agent i . The nominal configuration represents a general geometric pattern the agents are expected to achieve, and the time-varying target configuration is a continuous mapping from the nominal configuration to the target configuration through geometric transformations. We associate the nominal graph and the nominal configuration by a *nominal framework* $\mathcal{F} = (\mathcal{G}, \mathbf{P})$. A summary of the notations on the configurations is presented in Table I.

In the context of affine formation control, the transformation is limited to affine transformations which are characterized by a transformation matrix $\Theta_k^* \in \mathbb{R}^{D \times D}$ and a translation vector $\mathbf{t}_k^* \in \mathbb{R}^D$, where the superscript $*$ indicates a mapping for target configurations, which is subject to planning. The target configuration is then defined in global form by

$$\mathbf{Z}_k^* = \Theta_k^* \mathbf{P} + \mathbf{t}_k^* \mathbf{1}_N^T, \quad (2)$$

or from a local view of the i th agent $\forall i \in \mathcal{V}$, we have

$$\mathbf{z}_{i,k}^* = \Theta_k^* \mathbf{p}_i + \mathbf{t}_k^*. \quad (3)$$

From a geometric perspective, an affine transformation can be considered as a combination of basic geometric transformations including translation, scaling, rotation, and shearing, as shown in Fig. 1. In practice, certain geometric transformations and their combinations are special cases of affine transformation, which are widely applied in various scenarios. Correspondingly, the transformation matrix Θ_k^* is constrained to specific structures, and the degrees of freedom are reduced compared to general affine transformations. These properties will be explored in subsequent sections.

C. Formation Control Laws

The goal of formation control is to reach a desired geometric pattern [13], and maneuver control enables the agents to navigate in space with continuously changing geometric patterns [15]. The maneuverability is typically ensured by a technique called *leader-follower* strategy in which a small set \mathcal{V}_l of agents are set aside to be the *leaders* and the rest $\mathcal{V}_f = \mathcal{V} \setminus \mathcal{V}_l$ are the *followers*. The time-varying target formation is prescribed to the leaders while the followers only need to follow the leaders and stay in formation without any knowledge of the target configurations. In this work, we focus on the followers in the leader-follower approach as the leaders typically occupy a small portion of the nodes and are thus considered trivial.

Controller design regarding affine formation control are abundant in literature for different agent dynamics. For simplicity, we limit our discussion to single-integrator controllers i.e., $\dot{\mathbf{z}}_i = \mathbf{u}_i$ in a continuous form where \mathbf{u}_i is the velocity input, however our proposed approach can be applied, in general to any displacement-based controllers that depend on

TABLE II: A discrete-time adaptation of the control laws for undirected graphs [15]

Leaders	Control law
static	$\mathbf{u}_{i,k} = - \sum_{j \in \mathcal{N}_i} l_{ij} \mathbf{z}_{ij,k}$
constant velocity	$\mathbf{u}_{i,k} = -\alpha \sum_{j \in \mathcal{N}_i} l_{ij} \mathbf{z}_{ij,k} - \eta \sum_{\tau=0}^k \sum_{j \in \mathcal{N}_i} l_{ij} \mathbf{z}_{ij,\tau}$
varying velocity	$\mathbf{u}_{i,k} = -\frac{1}{\gamma_i} \sum_{j \in \mathcal{N}_i} l_{ij} (\mathbf{z}_{ij,k} - \dot{\mathbf{z}}_{j,k})$

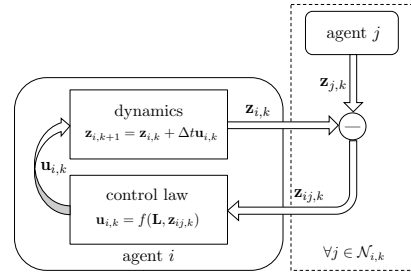


Fig. 3: An illustration of formation control under nominal graphs in discrete time [22]. The control law can be selected from Table II.

relative positions up to a translation. The discrete-time version of single-integrator dynamics is

$$\mathbf{z}_{i,k+1} = \mathbf{z}_{i,k} + \Delta t \mathbf{u}_{i,k} \quad \forall i \in \mathcal{V}, \quad (4)$$

where agents' positions are updated by the control input in a short time interval Δt . Some control input designs are shown in Table II, where $\mathbf{z}_{ij,k} = \mathbf{z}_{i,k} - \mathbf{z}_{j,k}$ in the table is the relative position up to a translation at time instance k which are modeled as the edges of the graph. Also, l_{ij} are elements of the stress matrix \mathbf{L} whose computation can be found in [13] and [15]. A diagram to illustrate the interactions in a formation control system is shown in Fig. 3. Following the control laws the agents can converge to and track the target positions from a random initialization.

D. Assumptions

We now make the following assumptions on the network for establishing stability.

Assumption 1 (*Communication graph and measurement graph*). We assume that the communication graph is the same as the measurement graph, i.e., no communication is established if the edge is unavailable in the functional graph.

This assumption is reasonable because the unavailability of observations is typically due to unreliable wireless channels in many cases as a large portion of relative localization methods are typically based on radio frequency signals [30].

Assumption 2 (*Stabilizability of an undirected framework*). The nominal framework $\mathcal{F} = (\mathcal{G}, \mathbf{P})$ is universally rigid such that the formation control system is stabilizable [13].

Assumption 2 has direct implications and conditions on the stress matrix \mathbf{L} used in the controller designs, which indicates the existence of a stabilizing controller.

III. PROBLEM FORMULATION

A. Motivation for Modeling Partial Observations

In the previous section, we emphasized the need for Assumption 2 for the stabilization of the existing controllers under undirected nominal graphs, which may not be readily satisfied by a network in reality. The cause for these situations usually involves communication constraints, e.g., bandwidth, communication radius, and sensor scheduling or malfunctioning. A few scenarios are discussed below and illustrated in Fig. 4.

1) *Directed functional graphs*: Since functional graphs \mathcal{G}_k are subgraphs of the undirected nominal graph, there can be cases where information flows only one way. In this case, pair (i, j) is a directed edge and the functional graph is a directed realization, as shown in Fig. 4(b). The controllers designed for directed topology cannot be applied in this case this issue can happen randomly and unexpectedly.

2) *Violation of stabilizing conditions*: A realization of the functional graph might not be universally rigid due to practical constraints, as shown in Fig. 4(c). A controller for affine formation stabilization is hard to design since it violates Assumption 2.

3) *Departing and rejoining agents*: A common practical case is where agents, due to maintenance, trajectory constraints, etc., cannot maintain the formation but have to temporarily or permanently depart from the swarm as shown in Fig. 4(d). This occurs frequently with satellites in space applications. In this case, the rest of the agents are still expected to maintain the formation until the same agent or its replacement returns or for the rest of the task.

B. Data Model

In this section, we provide an overview and modeling of the proposed framework in which we aim to estimate relative positions up to a translation $\mathbf{z}_{ij,k}$ for $(i, j) \in \mathcal{E} \setminus \mathcal{E}_k$. We first introduce general local relative (or edge) state-space modeling with the state variable $\gamma_{ij,k}$ for $(i, j) \in \mathcal{E}$ which includes the relative positions $\mathbf{z}_{ij,k}$ and relevant higher-order kinematics such as (relative) velocities and accelerations although for single-integrator controllers only relative positions are of primary concern. The state-space model adopts the form

$$\dot{\gamma}_{ij,k+1} = \mathbf{F}\gamma_{ij,k} + \mathbf{w}_{ij,k} \quad (5a)$$

$$\tilde{\mathbf{y}}_{ij,k} = \mathbf{G}\gamma_{ij,k} + \tilde{\mathbf{v}}_{ij,k}, \quad (5b)$$

where \mathbf{F} is the state transition matrix designed based on the assumed dynamics, \mathbf{G} is the selection matrix that maps full state variable to observations of relative positions, and $\mathbf{w}_{ij,k} \sim \mathcal{N}(\mathbf{0}, \mathbf{Q}_{ij})$ and $\tilde{\mathbf{v}}_{ij,k} \sim \mathcal{N}(\mathbf{0}, \tilde{\mathbf{R}}_{ij,k})$ are assumed to be zero-mean Gaussian. Note that, the dynamics in (5) provide the possibilities for standard tracking models such as constant acceleration, etc, and adaptive tracking algorithms, e.g., Kalman filters, can be used for estimation or prediction.

We now propose the following observation model to incorporate partial observations,

$$\tilde{\mathbf{y}}_{ij,k} = \begin{cases} \mathbf{y}_{ij,k}, & \text{if } (i, j) \in \mathcal{E}_k \\ \hat{\mathbf{z}}_{ij,k}^{\text{geo}}, & \text{if } (i, j) \in \mathcal{E} \setminus \mathcal{E}_k \end{cases}, \quad (6)$$

where

$$\mathbf{y}_{ij,k} = \mathbf{z}_{ij,k} + \mathbf{v}_{ij,k}, \quad (7)$$

is the observation available to agent i with noise $\mathbf{v}_{ij,k} \sim \mathcal{N}(\mathbf{0}, \mathbf{R}_{ij,k})$, and $\hat{\mathbf{z}}_{ij,k}^{\text{geo}}$ is an estimate using the geometry of formation if the observation $\mathbf{y}_{ij,k}$ cannot be made. This estimate is Gaussian with covariance $\mathbf{R}_{ij,k}^{\text{geo}} + \psi_{i,k}\mathbf{I}$ where $\mathbf{R}_{ij,k}^{\text{geo}}$ is the resulting covariance from a geometrical estimation and $\psi_{i,k}\mathbf{I}$ is our proposed novel adaptive penalty on the uncertainty reflecting the quality of $\hat{\mathbf{z}}_{ij,k}^{\text{geo}}$, which is discussed in detail later. As such, the observation-covariance pair $(\tilde{\mathbf{y}}_{ij,k}, \tilde{\mathbf{R}}_{ij,k})$ in the observation model (6) is either $(\mathbf{y}_{ij,k}, \mathbf{R}_{ij,k})$ or $(\hat{\mathbf{z}}_{ij,k}^{\text{geo}}, \mathbf{R}_{ij,k}^{\text{geo}} + \psi_{i,k}\mathbf{I})$ based on the availability of observation. An overview of the system architecture with partial observation and estimation is shown in Fig. 5 compared to the ideal case in Fig. 3. Next, we provide more details on $\hat{\mathbf{z}}_{ij,k}^{\text{geo}}$, the estimation using the geometry of the formation.

IV. ESTIMATION FROM GEOMETRY

The intuition behind geometric estimation is that the configuration space spanned by the positions of agents $\mathbf{Z}_{i,k}^*$ is mapped from a much smaller space described by the geometric parameters Θ_k^* and \mathbf{t}_k^* . Similar insights also hold for relative positions, thus they can be estimated by reconstructing the geometry parameters using part of the observed relative positions for the neighbors. We show that the relative positions are only dependent on the transformation matrix Θ_k^* which can be estimated using a simple least-square formulation. Then the unobserved relative positions can be reconstructed using the estimated Θ_k^* . This method is named relative affine localization (RAL) which has necessary conditions on the nominal configuration and the functional graph which can be violated in practice. We also propose techniques to relax these conditions and produce more accurate estimations by exploiting the geometry of formation or using neighborhood communication.

A. Relative Affine Localization

We first assume the case where the formation reaches sufficient convergence, i.e., $\mathbf{z}_{i,k} \rightarrow \mathbf{z}_{i,k}^*$ for $i \in \mathcal{V}$ and introduce the geometric estimation. In later sections, we discuss the modeling of sufficiency of convergence. Observe that

$$\mathbf{z}_{ij,k}^* = \mathbf{z}_{i,k}^* - \mathbf{z}_{j,k}^* = \Theta_k^* \mathbf{p}_i + \mathbf{t}_k^* - (\Theta_k^* \mathbf{p}_j + \mathbf{t}_k^*) = \Theta_k^* \mathbf{p}_{ij}, \quad (8)$$

where $\mathbf{p}_{ij} \triangleq \mathbf{p}_i - \mathbf{p}_j$ comes from the known nominal configuration. This means that the target relative positions $\mathbf{z}_{ij,k}^*$ are linear to Θ_k^* and so is $\mathbf{z}_{ij,k}$ upon sufficient convergence. From model (7), the observations can be written as $\mathbf{y}_{ij,k} = \mathbf{z}_{ij,k} + \mathbf{v}_{ij,k} = \Theta_k^* \mathbf{p}_{ij} + \mathbf{v}_{ij,k}$ which, by aggregating all available observations, leads to

$$\mathbf{Y}_{i,k} = \mathbf{X}_{i,k} + \mathbf{V}_{i,k} = \Theta_k^* \mathbf{H}_{i,k} + \mathbf{V}_{i,k}, \quad (9)$$

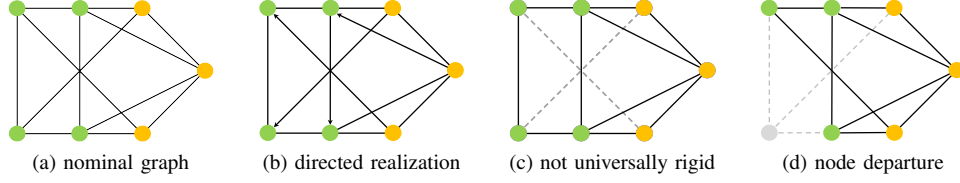


Fig. 4: Some practical scenarios relating to the functional graphs which are subgraphs of a nominal graph (a) [15]. Colored nodes and solid edges represent true agents and connections, and grey nodes and dashed edges are the unavailable agents and connections in the functional graph. Edges with arrows are directed edges pointing to nodes that receive information.

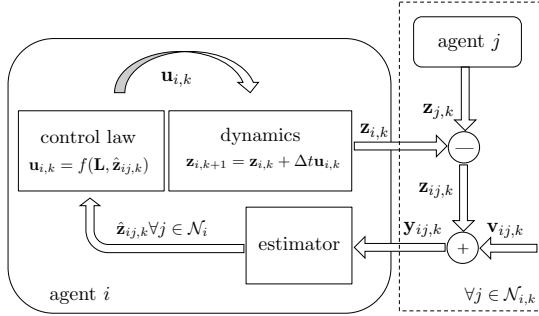


Fig. 5: An illustration of formation control under nominal graphs in discrete time. The control law can be selected from Table II.

where $\mathbf{X}_{i,k} \in \mathbb{R}^{D \times N_{i,k}}$ collects noiseless relative positions $\mathbf{z}_{ij,k}, \forall j \in \mathcal{N}_{i,k}$, $\mathbf{H}_{i,k} = \mathbf{P}\mathbf{B}_{i,k} \in \mathbb{R}^{D \times N_{i,k}}$ collects the corresponding relative nominal positions $\mathbf{p}_{ij}, \forall j \in \mathcal{N}_{i,k}$, and $\mathbf{V}_{i,k}$ is the noise matrix from $\mathbf{v}_{ij,k}$. An estimation of the geometric parameters Θ_k^* can be obtained by

$$\hat{\Theta}_{i,k} = \arg \min_{\Theta_k^*} \|\Theta_k^* \mathbf{H}_{i,k} - \mathbf{Y}_{i,k}\|_F^2 = \mathbf{Y}_{i,k} \Phi_{i,k}^T, \quad (10)$$

where $\Phi_{i,k} = (\mathbf{H}_{i,k} \mathbf{H}_{i,k}^T)^{-1} \mathbf{H}_{i,k}$. The geometric estimates $\hat{\mathbf{z}}_{ij,k}^{\text{geo}}, \forall j \in \mathcal{N}_i \setminus \mathcal{N}_{i,k}$ can be subsequently obtained by

$$\hat{\mathbf{z}}_{ij,k}^{\text{geo}} = \mathbf{Y}_{i,k} \Phi_{i,k}^T \mathbf{p}_{ij} \quad (11)$$

with a covariance structure

$$\mathbf{R}_{ij,k}^{\text{geo}} = (\mathbf{p}_{ij}^T \Phi_{i,k} \otimes \mathbf{I}_D) (\mathbf{I}_N \otimes \mathbf{R}_{ij}) (\mathbf{p}_{ij}^T \Phi_{i,k} \otimes \mathbf{I}_D)^T, \quad (12)$$

where \mathbf{R}_{ij} is the noise covariance for available observations from model (7), and this expression for $\mathbf{R}_{ij,k}^{\text{geo}}$ is derived in Appendix A. A unique solution using (11) is guaranteed if $\mathbf{H}_{i,k}$ is full row rank, which translates to some geometric conditions which we refer to as *geometric feasibility*.

Remark 1 (Geometric feasibility for RAL). Estimator (10) is geometrically feasible if and only if $\mathbf{Y}_{i,k}$ contains at least observations of D neighboring agents that are not collinear in \mathbb{R}^2 or coplanar in \mathbb{R}^3 in the nominal configuration.

Some examples are given in Fig. 6 to explain this feasibility further. As $\mathbf{H}_{i,k} = \mathbf{P}\mathbf{B}_{i,k}$, geometric feasibility can be decomposed into necessary conditions of \mathbf{P} and $\mathbf{B}_{i,k}$: configuration \mathbf{P} is *generic* [13] and $N_{i,k} \geq D$ meaning $\mathbf{B}_{i,k}$ has at least D columns. Another intuitive understanding of geometrical feasibility for RAL is the minimum number of independent

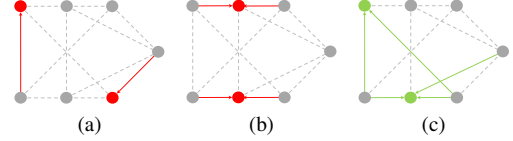


Fig. 6: Some examples to explain geometric feasibility of RAL in \mathbb{R}^2 . Colored nodes represent agents of interest. (a) infeasible due to $N_i^k < D$ locally. (b) infeasible due to collinear neighbors such that $\mathbf{H}_{i,k}$ is not full-rank. (c) feasible.

equations to solve for the parameters Θ^* in the underlying affine transformation.

Although geometric feasibility can be achieved in various scenarios, it can still be violated in loosely connected networks. To overcome this limitation, we introduce two approaches to relax the geometric feasibility for the broader applicability of the geometric estimator and more optimal estimations.

B. Constrained RAL

The first approach is when special cases of affine transformation are adopted and known to the agents. In practice, some maneuvers require specific transformations such as scaling only, rotation or similarity transforms. In these cases, the affine transformation matrix admits to a particular structure or presents some properties. By leveraging constraints on the formulation (10) the inversion in the solution to (10) can be avoided and thus the geometric feasibility is relaxed. An overview of these constrained problems and their solutions are shown in Table III, which are discussed in detail in the following. Using these constraints, the geometric feasibility is relaxed to 1 observation in the neighborhood for both $D = 2$ and $D = 3$.

Scaling. Scaling is an important feature of affine transformation that allows the swarm to pass through narrow passages or obstacles. For cases where only scaling is involved in the affine transformation, the parameter matrix Θ_k^* degenerates to

$$\Theta_k^* = \text{diag}(s_k^1, \dots, s_k^D), \quad (13)$$

where s_k^d , for $d = 1, \dots, D$, scales each dimension. Since the diagonality of Θ_k^* decouples the dimensions, the problem could be decomposed into D independent least squares problems and estimates \hat{s}_k^d for $d = 1, \dots, D$ can be easily given.

TABLE III: Solutions for Constrained RAL

	Scaling	Rotation	Similarity
constraints	Θ_k^* is diagonal	$\Theta_k^{*T} \Theta_k^* = \mathbf{I}_D$	$\Theta_k^{*T} \Theta_k^* = s_k^2 \mathbf{I}_D$
solutions	$\hat{\Theta}_{i,k} = \text{diag}(\hat{s}_{1,k}, \dots, \hat{s}_{D,k})$	$\mathbf{Y}_{i,k} \mathbf{H}_{i,k}^T = \mathbf{U}_{i,k} \Sigma_{i,k} \mathbf{V}_{i,k}^T$ $\hat{\Theta}_{i,k} = \mathbf{U}_{i,k} \mathbf{V}_{i,k}^T$	$\hat{s}_{i,k} = \frac{1}{D} \text{tr}(\Sigma_{i,k}^{H-1} \Sigma_{i,k}^Y)$ $\hat{\Theta}_{i,k} = \hat{s}_{i,k} \mathbf{U}_{i,k} \mathbf{V}_{i,k}^T$

Rotation. Rotation is a form of Euclidean transform that preserves the rigidity of the formation. It allows a collective change of orientation of the formation. The parameter matrix Θ_k^* in this case is a rotation matrix that is orthonormal as shown in Table III. This formulation is recognized as the orthogonal Procrustes problem [31] where an orthogonal matrix is sought to approximate rotations between two body frames. There are numerical and analytical solutions [32] available, and we adopt a singular value decomposition (SVD) based solution from [33].

Similarity. In similarity transforms all dimensions are uniformly scaled by a non-negative s_k on top of a rotation. Hence, the constraints on $\Theta_{i,k}$ can be relaxed from $\det(\Theta_{i,k}^*) = 1$ to $\det(\Theta_{i,k}^*) = s$, which then results in the formulation in Table III. The estimation can be based on the rotation estimation from the rotation case with an additional estimation on the scalar. If $\mathbf{H}_{i,k}$ and $\mathbf{Y}_{i,k}$ both have economy-sized SVD with $\Sigma_{i,k}^H$ and $\Sigma_{i,k}^Y$ as the respective diagonal matrices, the scalar can be estimated by dividing the energies on each (rotated) dimension before and after transformation.

C. Consensus Filtering

Another approach to relax geometric feasibility is to use the estimated Θ_k^* from neighbors. In essence, the geometry parameters Θ_k^* can be considered latent parameters which are estimated by RAL using a consensus process. As such, distributed filtering and fusion across the network can also be applied in the latent space for two purposes: reducing the noise of the estimated $\hat{\Theta}_{i,k}$ and sharing the estimates in case geometric feasibility is violated. We propose the use of a well-established dynamic consensus filtering protocol as follows [34]:

$$\hat{\Theta}_{i,k+1}^{\text{con}} = \hat{\Theta}_{i,k}^{\text{con}} + \epsilon \left[\sum_{j \in \mathcal{N}_i} (\hat{\Theta}_{j,k}^{\text{con}} - \hat{\Theta}_{i,k}^{\text{con}}) + \sum_{j \in \mathcal{J}_{i,k}} (\hat{\Theta}_{j,k} - \hat{\Theta}_{i,k}^{\text{con}}) \right], \quad (14)$$

where $\hat{\Theta}_{j,k}$ are estimates from RAL and ϵ is a known small value. Here, $\mathcal{J}_{i,k}$ is the union set of the neighbors and node i , i.e., $\mathcal{J}_{i,k} = \mathcal{N}_{i,k} \cup \{i\}$.

V. LOCAL CONVERGENCE INDICATOR

In the previous section we assumed the formation has sufficiently converged i.e., $\mathbf{z}_{i,k} \rightarrow \mathbf{z}_{i,k}^*$ for $i \in \mathcal{V}$, to derive the geometrical estimators, however, this is not assumed to be the case upon the initialization of the configuration. Similar scenarios could also occur when large environmental disturbances, e.g., gusts, temporarily deform the converged configuration. Therefore, the geometric estimators may not

be accurate until the system converges, which is why our proposed model (6) introduces an adaptive penalty $\psi_{i,k} \mathbf{I}$ for the covariance of the geometric estimates $\hat{\mathbf{z}}_{i,j,k}^{\text{geo}}$ to account for the error and $\psi_{i,k}$ is a local convergence indicator (CI) to gauge the sufficiency of convergence.

An ideal indicator function would be the tracking error

$$\delta_k = \frac{1}{N} \|\mathbf{Z}_k - \mathbf{Z}_k^*\|_F^2, \quad (15)$$

which is commonly used in literature to indicate convergence and steady-state error [15], [17], [35], [36]. However, this is a global function by nature and thus is locally intractable. In addition, neither the absolute positions in \mathbf{Z}_k nor the target configuration are assumed to be known to the follower agents, which makes it infeasible to calculate. We therefore propose the following CI

$$\psi_{i,k} = \frac{1}{N_{i,k}} \sum_{j \in \mathcal{N}_{i,k}} \left\| \hat{\Theta}_{i,k} - \hat{\Theta}_{j,k} \right\|_F^2, \quad (16)$$

where $\hat{\Theta}_{i,k}$ is a local estimate of the geometry parameters using (10), and $\hat{\Theta}_{j,k}$ shall be accessible through neighborhood communication. In contrast to (15), our proposed CI (16) requires no global information but exhibits a similar trend as the tracking error δ_k . Intuitively, this function measures the difference between the estimates of the geometry parameters. If the system has converged to an affine formation, these estimates shall reach a consensus, which is illustrated in Fig. 7. In the following theorem and corollary, we show the relationship between $\psi_{i,k}$ and δ_k , which leads to a claim on the convergence guarantees CI.

Theorem 1 (*Upper bound of the convergence indicator*). In the noiseless case, the local convergence indicator function $\psi_{i,k}$ defined in (16) is upper bounded by the tracking error δ_k in (15) i.e., $\psi_{i,k} \leq c_{i,k} \delta_k$, where $c_{i,k}$ is a time-varying scaling factor given by

$$c_{i,k} = \frac{N}{N_{i,k}} \sum_{j \in \mathcal{N}_{i,k}} \left\| \mathbf{B}_{i,k} \Phi_i^T - \mathbf{B}_{j,k} \Phi_j^T \right\|_F^2. \quad (17)$$

Proof. See Appendix B-A ■

Theorem 1 shows, that if the tracking error δ_k asymptotically and exponentially converges to zero under some control protocols, the local indicator $\psi_{i,k}$ will also converge similarly up to a known scalar. In the noisy case, it can be intuitively speculated that similar conclusions hold for the expectation of the functions, which is formalized in the following.

Corollary 1 (*Upper bound of CI under observation noises*). Under observation model (9), the expectation of the local convergence indicator $\mathbb{E}[\psi_{i,k}]$ is upper bounded by the expectation

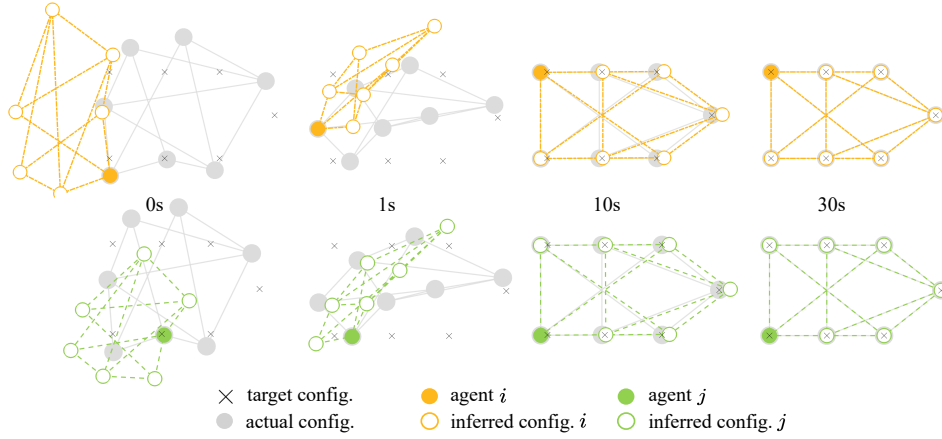


Fig. 7: Illustration of the convergence indicator. While the system has not sufficiently converged, e.g., at 0s or 1s, large discrepancies of $\hat{\Theta}_{i,k}$ lead to different locally perceived formations, i.e., the inferred configuration $\hat{\Theta}_{i,k}\mathbf{P}$. As the system converges to the target configuration, these discrepancies decrease till agents reach a consensus on the perceived formation at e.g., 30s.

of the tracking error $\mathbb{E}[\delta_k]$ up to a scaling factor and an offset, i.e., $\mathbb{E}[\psi_{i,k}] \leq c_{i,k}\mathbb{E}[\delta_k] + b_{i,k}$, where

$$c_{i,k} = \frac{N}{N_{i,k}} \sum_{j \in \mathcal{N}_{i,k}} \|\Phi_{i,k} \mathbf{B}_{i,k}^T - \Phi_{j,k} \mathbf{B}_{j,k}^T\|_F^2, \quad (18a)$$

$$b_{i,k} = \frac{\text{tr}[\mathbf{R}_{ij}]}{N_{i,k}} \sum_{j \in \mathcal{N}_{i,k}} (\|\Phi_{i,k}\|_F^2 + \|\Phi_{j,k}\|_F^2). \quad (18b)$$

Proof. See Appendix B-B. ■

When noise is present, a biased term related to the covariance of the noise appears in the inequality. In this case, we claim that if the noise energy is finite and the tracking error is converging to zero, CI also converges to a finite value.

It should be noted from the definition of CI (16) only requires agreement on the estimated parameter matrix in the neighborhood to reach zero. This means $\psi_{i,k} = 0$ for any configuration $\mathbf{Z}_k = \mathbf{Z}_k^*$ up to an affine transformation. For instance, if the system converges to the target configuration up to a large translation, indicators $\psi_{i,k}$ for all i will be zero but the tracking error will be large, which makes the convergence for $\delta_k \rightarrow 0$ a sufficient but not necessary condition for the convergence $\psi_{i,k} \rightarrow 0$ as described. As such, CI should be generally considered a shape convergence indicator rather than a maneuver indicator. In practice, as the setting of leaders will ensure convergence of target configuration, we can use $\psi_{i,k}$ to locally refer to global convergence.

VI. ALGORITHMS

We now summarize our proposed solution, which is a fusion of temporal information using a Kalman filter and spatial information from the geometry of the affine formation in a general form, and it constitutes the "estimator" block in Fig. 5. In summary, we present 3 algorithms, relative Kalman filtering (RKF), relative affine localization (RAL) with consensus filtering (conRAL), and geometry-aware RKF (GA-RKF), which can all be derived from model (5) and (6).

A. Case 1: Relative Kalman Filtering

We first discuss the relative state-space model (5), where we consider a constant acceleration model. The matrices in (5) are then

$$\mathbf{G} = \mathbf{I}_D \otimes [1 \ 0 \ 0], \quad (19)$$

$$\mathbf{F} = \mathbf{I}_D \otimes \begin{bmatrix} 1 & \Delta t & \frac{1}{2} \Delta t^2 \\ 0 & 1 & \Delta t \\ 0 & 0 & 1 \end{bmatrix}, \quad (20)$$

$$\mathbf{Q}_{ij} = \sigma_w^2 \mathbf{I}_D \otimes \begin{bmatrix} \frac{\Delta t^4}{4} & \frac{\Delta t^3}{2} & \frac{\Delta t^2}{2} \\ \frac{\Delta t^3}{2} & \Delta t^2 & \Delta t \\ \frac{\Delta t^2}{2} & \Delta t & 1 \end{bmatrix}, \quad (21)$$

where σ_w^2 is the variance of acceleration uncertainty, which can be further tuned. The covariance structure can be derived by projecting small deflections of acceleration in the state vector. Algorithm 1 describes the proposed relative Kalman filter (RKF), which is a direct adaptation of the Kalman filtering under intermittent observations [37] to our relative state-space model (5) for affine formation control. It propagates the dynamic model to predict without correction from the observations if they are unavailable.

This algorithm, as we will show in the simulation section, is robust to random losses of observations since the dynamic model can capture some motion information of the agent and predictions can be made when necessary. In practice, relative state-space modeling can also be done using other models or combinations of models such as interactive multiple models (IMM) for better approximation.

B. Case 2: RAL with Consensus Filtering

Similar to the Kalman filtering, RAL-based algorithms can also be stand-alone estimators. Here we introduce an improved version that concatenates RAL with the consensus filtering protocol, which mitigates the constraint of geometric feasibility, in scenarios when estimators may not exist due to insufficient observations.

Algorithm 1 *Relative Kalman filtering (RKF)*

```

1: Initialize  $\hat{\gamma}_{ij,0|0}$ ,  $\Sigma_{ij,0|0}$ ,  $\mathbf{R}_{ij}$ , and  $\mathbf{Q}_{ij}$ 
2: Locally compute for all agent  $i$  and all time  $k$ 
3: for  $j \in \mathcal{N}_i$  do ▷ Prediction
4:    $\hat{\gamma}_{ij,k|k-1} = \mathbf{F}\hat{\gamma}_{ij,k-1|k-1}$ 
5:    $\Sigma_{ij,k|k-1} = \mathbf{F}\Sigma_{ij,k-1|k-1}\mathbf{F}^T + \mathbf{Q}_{ij}$ 
6:   if  $(i, j) \in \mathcal{E}_k$  then ▷ Correction
7:      $\mathbf{K}_{ij,k} = \Sigma_{ij,k|k-1}\mathbf{G}^T(\mathbf{R}_{ij} + \mathbf{G}\Sigma_{ij,k|k-1}\mathbf{G}^T)^{-1}$ 
8:      $\hat{\gamma}_{ij,k|k} = \hat{\gamma}_{ij,k|k-1} + \mathbf{K}_{ij,k}(\mathbf{y}_{ij,k} - \mathbf{G}\hat{\gamma}_{ij,k|k-1})$ 
9:      $\Sigma_{ij,k|k} = (\mathbf{I} - \mathbf{K}_{ij,k}\mathbf{G})\Sigma_{ij,k|k-1}$ 
10:   else ▷ Propagation
11:      $\hat{\gamma}_{ij,k|k} = \hat{\gamma}_{ij,k|k-1}$ 
12:      $\Sigma_{ij,k|k} = \Sigma_{ij,k|k-1}$ 
13:   end if
14:    $\hat{\mathbf{z}}_{ij,k} = \mathbf{G}\hat{\gamma}_{ij,k|k}$  ▷ Extract positions
15: end for

```

Algorithm 2 *RAL with consensus filtering (conRAL)*

```

1: For all time instance  $k$ 
2: Initialize  $\hat{\Theta}_{i,k} = 0$ 
3: Locally compute for all agent  $i$ 
4: if  $\text{rank}(\mathbf{H}_{i,k}) = D$  then ▷ geometric feasibility
5:    $\hat{\Theta}_{i,k} = \mathbf{Y}_{i,k}\Phi_{i,k}^T$ 
6: end if
7: exchange  $\hat{\Theta}_{i,k}$  in the neighborhood
8: compute  $\hat{\Theta}_{i,k}^{\text{con}}$  using (14) ▷ consensus filtering
9: for  $j \in \mathcal{N}_i$  do
10:   if  $(i, j) \in \mathcal{E}_k$  then
11:      $\hat{\mathbf{z}}_{ij,k} = \hat{\Theta}_{i,k}^{\text{con}}\mathbf{P}_{ij}$ 
12:   end if
13: end for

```

In Algorithm 2, if the algorithm does not execute consensus filtering and simply adopt $\hat{\mathbf{z}}_{ij,k} = \hat{\Theta}_{i,k}\mathbf{P}_{ij}$, a standard RAL is performed. In addition, if geometric feasibility does not hold but the system is adopting special cases of affine transformations and is known as prior knowledge, the computation of $\hat{\Theta}_{i,k}$ can be done using solutions from Table III instead. The performance of this algorithm depends on the quality of the estimation of $\hat{\Theta}_{i,k}$ and is particularly useful in case of node departures. In these cases, the neighboring agents will estimate the missing edges as if they are still active.

C. Case 3: Geometry-Aware Kalman Filtering

Algorithm 3 gives the details of the fusion of RAL-based algorithms and RKF. Using the full proposed framework, RAL estimates are computed first, which can be treated as alternative observations for unavailable edges for the Kalman filter. The consensus indicators are also computed prior to the filtering step, which is then used to weigh the uncertainty of the RAL estimates. Note that, the Algorithm 3 reduces to Algorithm 1 if RAL cannot be performed due to geometric feasibility.

Algorithm 3 *Geometry-aware RKF (GA-RKF)*

```

1: Initialize RKF and RAL as in Algorithm 1 and 2
2: Locally compute for all agent  $i$  and time instances  $k$ 
3: if  $\text{rank}(\mathbf{H}_{i,k}) = D$  then ▷ geometric feasibility
4:    $\hat{\Theta}_{i,k} = \mathbf{Y}_{i,k}\Phi_{i,k}^T$ 
5: end if
6: Exchange  $\hat{\Theta}_{i,k}$  and compute  $\psi_{i,k}$ 
7: for  $j \in \mathcal{N}_i$  do
8:    $\hat{\mathbf{z}}_{ij,k}^{\text{geo}} = \hat{\Theta}_{i,k}\mathbf{P}_{ij}$ 
9:   Build observation model (6)
10:  if  $(i, j) \in \mathcal{E}_k$  or RAL feasible then
11:     $\mathbf{K}_{ij,k} = \Sigma_{ij,k|k-1}\mathbf{G}^T(\hat{\mathbf{R}}_{ij} + \mathbf{G}\Sigma_{ij,k|k-1}\mathbf{G}^T)^{-1}$ 
12:     $\hat{\gamma}_{ij,k|k} = \hat{\gamma}_{ij,k|k-1} + \mathbf{K}_{ij,k}(\tilde{\mathbf{y}}_{ij,k} - \mathbf{G}\hat{\gamma}_{ij,k|k-1})$ 
13:     $\Sigma_{ij,k|k} = (\mathbf{I} - \mathbf{K}_{ij,k}\mathbf{G})\Sigma_{ij,k|k-1}$ 
14:  else ▷ Propagation
15:     $\hat{\gamma}_{ij,k|k} = \hat{\gamma}_{ij,k|k-1}$ 
16:     $\Sigma_{ij,k|k} = \Sigma_{ij,k|k-1}$ 
17:  end if
18:   $\hat{\mathbf{z}}_{ij,k} = \mathbf{G}\hat{\gamma}_{ij,k|k}$  ▷ Extract positions
19: end for

```

VII. SIMULATIONS

In this section, we present numerical validations of several practical scenarios to show the enhanced robustness of using our proposed algorithms.

A. Simulation Setup

We consider two formations in Fig. 9 presented in the literature [1], [15]. Graph 1 has $N = 7$ nodes with $M/2 = 12$ undirected edges and Graph 2 has $N = 10$ nodes with $M/2 = 30$ undirected edges. They are selected for the simulations as they feature different densities of connections indicated by algebraic connectivity (a.c.). The more sparsely connected formations are considered more susceptible to being unstabilizable under time-varying functional graphs with loss of information. We intend to show that our proposed algorithms work for both formations.

The maneuvering pattern used in the simulation is shown in Fig. 8 where the duration of the simulation is 60s and the time step Δt is chosen as 0.01s meaning 6000 discrete time instances k in total. For all the results on the tracking error (15), 50 Monte Carlo simulations are run for each discrete time instance and averaged over the number of simulations, unless otherwise indicated. The noise covariance $\mathbf{R}_{ij,k}$ for the observation model (7) is chosen as a constant $\sigma_v^2\mathbf{I}, \forall k$ where σ_v is selected as 0.1.

B. Convergence Indicator

In Section V, we showed that the convergence indicator (16) is upper bounded by the tracking error (15) through Theorem 1 and Corollary 1. We first show the result of the convergence indicator in Fig. 10. Here, we present the tracking error in black and the convergence of CI for each follower in color using Graph 1. To give a direct comparison, the CIs are corrected with their corresponding coefficients $b_{i,k}$

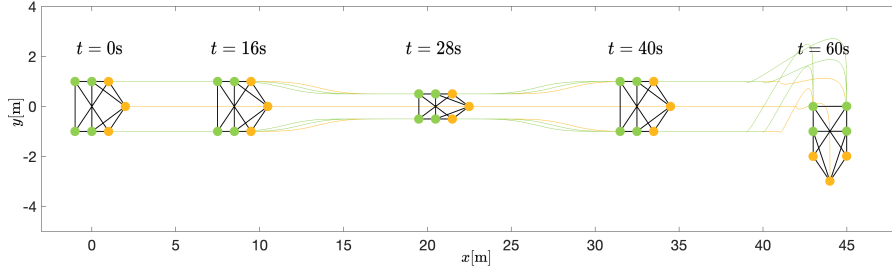


Fig. 8: The target trajectories which is also used in [15].

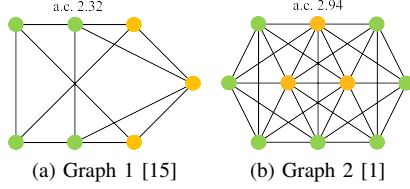


Fig. 9: The nominal graphs used in the simulation with their algebraic connectivity (a.c.). Both are universally rigid for affine formation control. Graph 2 has higher algebraic connectivity meaning a denser connection among the nodes and more information exchange in the network.

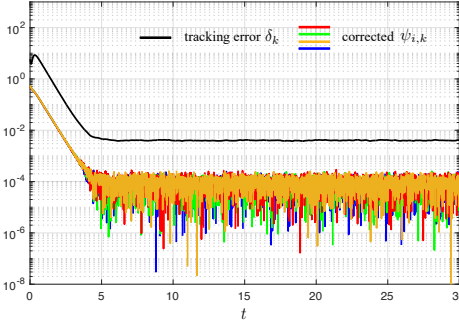
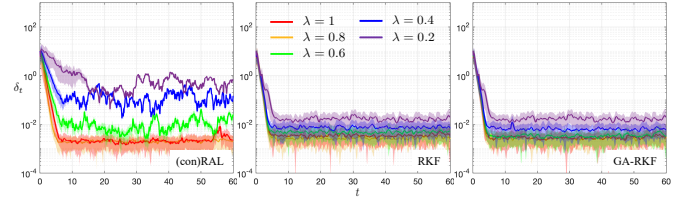


Fig. 10: The convergence of CI and the tracking error. The black line is the mean tracking error δ_k and the colored lines are the mean corrected indicators $(\psi_{i,k} - b_i)/c_i$ for each follower. 1000 Monte Carlo runs are performed for this simulation to approximate the expectation of the functions.

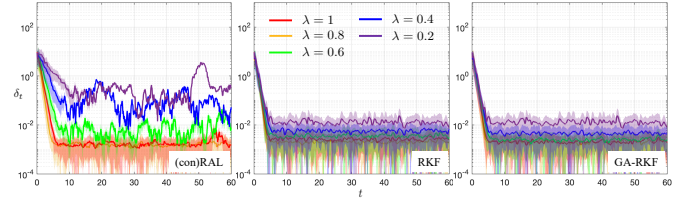
and $c_{i,k}$ which are time-invariant in this example as we use nominal graphs with any observation losses. As can be seen from the figure, the corrected CI is always upper-bounded by the tracking error which substantiates Corollary 1. Another observation from Fig. 10 is that the CI follows the tracking error which makes it a reasonable local approximator. In the case of time-varying graphs, the variance of CI could be larger than shown in Fig. 10, but remains upper bounded to the tracking error.

C. Random Observation Losses

If the observation loss occurs randomly, we model its availability using a Bernoulli distribution with probability λ . Larger values of λ indicate fewer losses on average for each edge over time. $\lambda = 1$ means the functional graphs are the



(a) Graph 1



(b) Graph 2

Fig. 11: Convergence plots of the example algorithms for several choices of λ . Solid lines represent the mean of all Monte Carlo runs, and the translucent area is the ± 1 standard deviation region.

same as the nominal graph and no edge losses are present. The proposed algorithms for both graphs in Fig. 9 with different choices of λ are shown in Fig. 11 where the convergence of Algorithm 1-3 is shown. Two focuses should be made w.r.t these convergence curves: one is the steady-state error and the other is the convergence speed. In general, the larger λ is, the more available edges, thus the better performance in both convergence speed and steady-state error. Compared to using only geometry information in Algorithm 1 (conRAL), RKF-based algorithms are more capable of dealing with low observation availabilities with a convergence speed nearly the same as the $\lambda = 1$ case. This can be also verified in Fig. 12 (a) and (b) where the mean tracking error (δ_k averaged across the duration of simulation) is compared for the algorithms across different choices of λ . It can be seen that the curves for RKF and GA-RKF are almost flat across λ meaning that they are strongly robust to random losses of observations whereas conRAL deteriorates to the no estimator case as λ gets smaller.

D. Switching Topologies with Node Departures

We show a few topology switching cases for both nominal graphs as shown in Fig. 12 (c) and (d). Here, we test the ability of our proposed estimators to maintain stability. As can be seen, the "no estimator" case and RKF diverge with

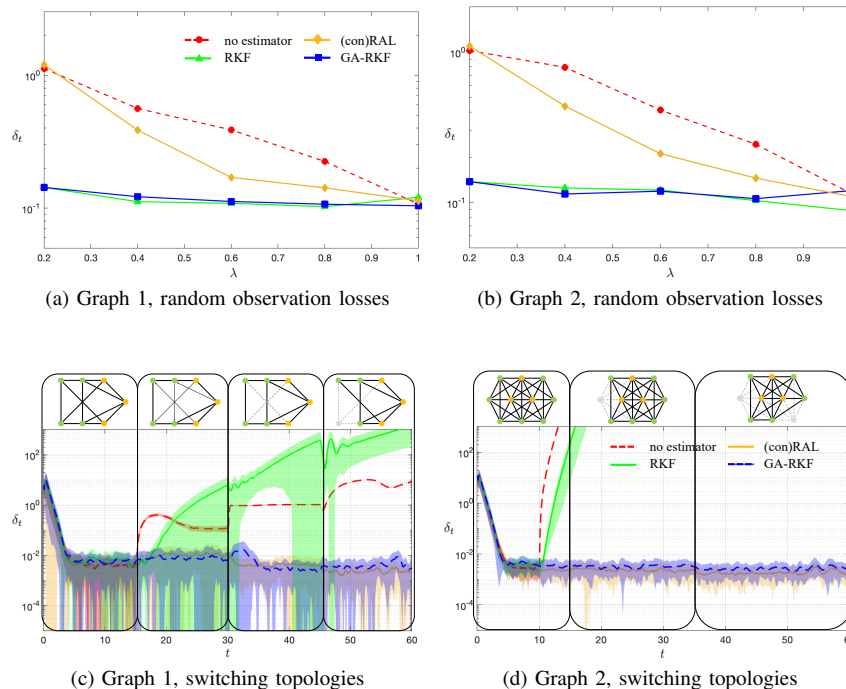


Fig. 12: Mean tracking error across λ for the random loss scenario (a) and (b). The convergence plot for switching topologies (c) and (d). The graphs are plotted involving directed realizations of an undirected graph, missing edges, and node departures. The plots are also partitioned accordingly based on the simulation period for each topology.

topology change whereas conRAL and GA-RKF maintain the convergence. The reason for the divergence of "no estimator" is that the underlying graph changes result in different stress matrices for the controller and the new stress matrices do not necessarily exist due to the rigidity requirement. For the RKF, the predictions are outdated as soon as the relative dynamics change without the correction of observations. As such, a simple maneuver of the systems can cause instability. On the other hand, since the geometry estimation is still accurate as the edge losses and node departures do not instantly corrupt the geometric pattern, our proposed estimators conRAL and GA-RKF can maintain the converged state. Therefore, they are considered robust to switching topologies, as compared to RKF.

VIII. CONCLUSION

In this paper, we proposed an estimation framework to enhance the robustness of affine formation control to the loss of observations which are modeled as time-varying functional graphs. Our framework fuses estimators using both temporal and spatial (geometrical) information and is also flexible to exploit these estimators individually. Some example algorithms are presented under the proposed framework and we presented simulations for different types of time-varying graphs. In particular, the geometry-aware relative Kalman filtering (GA-RKF) is proven to be robust for all presented scenarios. In our future work, we aim to further strengthen several aspects of our proposed framework. First, the discussions are limited to the edges availability and node departures w.r.t. followers. Furthermore, theoretical guarantees on the stability of the

formation control using such an estimation framework should be investigated.

REFERENCES

- [1] Z. Li and R. T. Rajan, "Geometry-aware distributed kalman filtering for affine formation control under observation losses," in *2023 26th International Conference on Information Fusion (FUSION)*, 2023, pp. 1–7.
- [2] A. Heuillet, F. Couthouis, and N. Díaz-Rodríguez, "Collective explainable ai: Explaining cooperative strategies and agent contribution in multiagent reinforcement learning with shapley values," *IEEE Computational Intelligence Magazine*, vol. 17, no. 1, pp. 59–71, 2022.
- [3] Y. Rizk, M. Awad, and E. W. Tunstel, "Cooperative heterogeneous multi-robot systems: A survey," *ACM Computing Surveys (CSUR)*, vol. 52, no. 2, pp. 1–31, 2019.
- [4] R. Ureña, G. Kou, Y. Dong, F. Chiclana, and E. Herrera-Viedma, "A review on trust propagation and opinion dynamics in social networks and group decision making frameworks," *Information Sciences*, vol. 478, pp. 461–475, 2019. [Online]. Available: <https://www.sciencedirect.com/science/article/pii/S0020025518309253>
- [5] G. Zhao, H. Cui, and C. Hua, "Hybrid event-triggered bipartite consensus control of multiagent systems and application to satellite formation," *IEEE Transactions on Automation Science and Engineering*, vol. 20, no. 3, pp. 1760–1771, 2023.
- [6] J. Alonso-Mora, S. Baker, and D. Rus, "Multi-robot formation control and object transport in dynamic environments via constrained optimization," *The International Journal of Robotics Research*, vol. 36, no. 9, pp. 1000–1021, 2017. [Online]. Available: <https://doi.org/10.1177/0278364917719333>
- [7] G.-P. Liu and S. Zhang, "A survey on formation control of small satellites," *Proceedings of the IEEE*, vol. 106, no. 3, pp. 440–457, 2018.
- [8] K. A. Ghamry and Y. Zhang, "Cooperative control of multiple uavs for forest fire monitoring and detection," in *2016 12th IEEE/ASME International Conference on Mechatronic and Embedded Systems and Applications (MESA)*, 2016, pp. 1–6.
- [9] S.-M. Kang, M.-C. Park, B.-H. Lee, and H.-S. Ahn, "Distance-based formation control with a single moving leader," in *2014 American Control Conference*, 2014, pp. 305–310.

- [10] D. Van Vu, M. H. Trinh, P. D. Nguyen, and H.-S. Ahn, "Distance-based formation control with bounded disturbances," *IEEE Control Systems Letters*, vol. 5, no. 2, pp. 451–456, 2021.
- [11] S. Zhao and D. Zelazo, "Translational and scaling formation maneuver control via a bearing-based approach," *IEEE Transactions on Control of Network Systems*, vol. 4, no. 3, pp. 429–438, 2017.
- [12] J. Zhao, X. Li, X. Yu, and H. Wang, "Finite-time cooperative control for bearing-defined leader-following formation of multiple double-integrators," *IEEE Transactions on Cybernetics*, vol. 52, no. 12, pp. 13 363–13 372, 2022.
- [13] Z. Lin, L. Wang, Z. Chen, M. Fu, and Z. Han, "Necessary and sufficient graphical conditions for affine formation control," *IEEE Transactions on Automatic Control*, vol. 61, no. 10, pp. 2877–2891, 2016.
- [14] P. Zhang, D. Ma, P. Liu, and M. Li, "Robust affine maneuver formation control based of second-order multi-agent grid inspection systems," *Frontiers in Energy Research*, vol. 10, 2022. [Online]. Available: <https://www.frontiersin.org/articles/10.3389/fenrg.2022.972999>
- [15] S. Zhao, "Affine formation maneuver control of multiagent systems," *IEEE Transactions on Automatic Control*, vol. 63, no. 12, pp. 4140–4155, 2018.
- [16] L. Wang, Z. Lin, and M. Fu, "Affine formation of multi-agent systems over directed graphs," in *53rd IEEE Conference on Decision and Control*, 2014, pp. 3017–3022.
- [17] Y. Xu, S. Zhao, D. Luo, and Y. You, "Affine formation maneuver control of multi-agent systems with directed interaction graphs," in *2018 37th Chinese Control Conference (CCC)*, 2018, pp. 4563–4568.
- [18] —, "Affine formation maneuver control of linear multi-agent systems with undirected interaction graphs," in *2018 IEEE Conference on Decision and Control (CDC)*, 2018, pp. 502–507.
- [19] Y. Lin, Z. Lin, Z. Sun, and B. D. O. Anderson, "A unified approach for finite-time global stabilization of affine, rigid, and translational formation," *IEEE Transactions on Automatic Control*, vol. 67, no. 4, pp. 1869–1881, 2022.
- [20] H. G. de Marina, J. Jimenez Castellanos, and W. Yao, "Leaderless collective motions in affine formation control," in *2021 60th IEEE Conference on Decision and Control (CDC)*, 2021, pp. 6433–6438.
- [21] C. Garanayak and D. Mukherjee, "Leaderless affine formation maneuvers over directed graphs," in *2022 IEEE 61st Conference on Decision and Control (CDC)*, 2022, pp. 3983–3988.
- [22] M. Van Der Marel and R. T. Rajan, "Distributed kalman filters for relative formation control of multi-agent systems," in *2022 30th European Signal Processing Conference (EUSIPCO)*, 2022, pp. 1422–1426.
- [23] T. Han, Z. Lin, R. Zheng, and M. Fu, "A barycentric coordinate-based approach to formation control under directed and switching sensing graphs," *IEEE Transactions on Cybernetics*, vol. 48, no. 4, pp. 1202–1215, 2018.
- [24] X. Dong and G. Hu, "Time-varying formation control for general linear multi-agent systems with switching directed topologies," *Automatica*, vol. 73, pp. 47–55, 2016. [Online]. Available: <https://www.sciencedirect.com/science/article/pii/S0005109816302515>
- [25] Z. Wang, T. Liu, and Z.-P. Jiang, "Cooperative formation control under switching topology: An experimental case study in multirotors," *IEEE Transactions on Cybernetics*, vol. 51, no. 12, pp. 6141–6153, 2021.
- [26] G. Franzè, A. Casavola, D. Famularo, and W. Lucia, "Distributed receding horizon control of constrained networked leader–follower formations subject to packet dropouts," *IEEE Transactions on Control Systems Technology*, vol. 26, no. 5, pp. 1798–1809, 2018.
- [27] X. Gong, Y.-J. Pan, J.-N. Li, and H. Su, "Leader following consensus for multi-agent systems with stochastic packet dropout," in *2013 10th IEEE International Conference on Control and Automation (ICCA)*, 2013, pp. 1160–1165.
- [28] L. Sedghi, J. John, M. Noor-A-Rahim, and D. Pesch, "Formation control of automated guided vehicles in the presence of packet loss," *Sensors*, vol. 22, no. 9, 2022. [Online]. Available: <https://www.mdpi.com/1424-8220/22/9/3552>
- [29] J. Lee, S.-Y. Park, D.-E. Kang *et al.*, "Relative navigation with intermittent laser-based measurement for spacecraft formation flying," *Journal of Astronomy and Space Sciences*, vol. 35, no. 3, pp. 163–173, 2018.
- [30] S. Chen, D. Yin, and Y. Niu, "A survey of robot swarms' relative localization method," *Sensors*, vol. 22, no. 12, 2022. [Online]. Available: <https://www.mdpi.com/1424-8220/22/12/4424>
- [31] S. Prince, *Computer Vision: Models Learning and Inference*. Cambridge University Press, 2012.
- [32] T. Viklands, "Algorithms for the weighted orthogonal procrustes problem and other least squares problems," Ph.D. dissertation, Datavetenskap, 2006. [Online]. Available: <https://api.semanticscholar.org/CorpusID:6919969>
- [33] P. H. Schönemann, "A generalized solution of the orthogonal procrustes problem," *Psychometrika*, vol. 31, pp. 1–10, 1966. [Online]. Available: <https://api.semanticscholar.org/CorpusID:121676935>
- [34] R. Olfati-Saber and J. Shamma, "Consensus filters for sensor networks and distributed sensor fusion," in *Proceedings of the 44th IEEE Conference on Decision and Control*, 2005, pp. 6698–6703.
- [35] H. Su, Z. Yang, S. Zhu, and C. Chen, "Bearing-based formation maneuver control of leader-follower multi-agent systems," *IEEE Control Systems Letters*, vol. 7, pp. 1554–1559, 2023.
- [36] F. Xiao, Q. Yang, X. Zhao, and H. Fang, "A framework for optimized topology design and leader selection in affine formation control," *IEEE Robotics and Automation Letters*, vol. 7, no. 4, pp. 8627–8634, 2022.
- [37] B. Sinopoli, L. Schenato, M. Franceschetti, K. Poolla, M. Jordan, and S. Sastry, "Kalman filtering with intermittent observations," *IEEE Transactions on Automatic Control*, vol. 49, no. 9, pp. 1453–1464, 2004.
- [38] K. B. Petersen, M. S. Pedersen *et al.*, "The matrix cookbook," *Technical University of Denmark*, vol. 7, no. 15, p. 510, 2008.

APPENDIX A

DERIVATION OF THE COVARIANCE FOR (12)

Given model (9) and estimator (11), we have

$$\hat{\mathbf{z}}_{ij,k}^{\text{geo}} = \mathbf{Y}_{i,k} \Phi_{i,k}^T \mathbf{p}_{ij} = (\mathbf{X}_{i,k} + \mathbf{V}_{i,k}) \Phi_{i,k}^T \mathbf{p}_{ij}, \quad (22)$$

where $\mathbf{V}_{i,k}$ is stochastic. Employing the property of vectorization and the Kronecker product (see (520) in [38]), then we have

$$\text{cov}[\hat{\mathbf{z}}_{ij,k}^{\text{geo}}] = \text{cov}[\text{vec}(\hat{\mathbf{z}}_{ij,k}^{\text{geo}})] = \text{cov}[\text{vec}(\mathbf{V}_{i,k} \Phi_{i,k}^T \mathbf{p}_{ij})] \quad (23a)$$

$$= \text{cov}[(\mathbf{p}_{ij}^T \Phi_{i,k} \otimes \mathbf{I}_D) \text{vec}(\mathbf{V}_{i,k})] \quad (23b)$$

$$= \bar{\Phi}_{i,k} \text{cov}[\text{vec}(\mathbf{V}_{i,k})] \bar{\Phi}_{i,k}^T \quad (23c)$$

$$= \bar{\Phi}_{i,k} (\mathbf{I} \otimes \mathbf{R}_{ij}) \bar{\Phi}_{i,k}^T, \quad (23d)$$

where we introduce $\bar{\Phi}_{i,k} = (\mathbf{p}_{ij}^T \Phi_{i,k} \otimes \mathbf{I}_D)$ and $\text{vec}(\mathbf{V}_{i,k})$ collects zero-mean i.i.d. noise vectors with covariance \mathbf{R}_{ij} .

APPENDIX B

CONVERGENCE INDICATOR

A. Proof of Theorem 1

Proof. In the noiseless case, note that the solution to (10) becomes $\hat{\Theta}_{i,k} = \mathbf{X}_{i,k} \Phi_{i,k}^T = \mathbf{Z}_k \mathbf{B}_{i,k} \Phi_{i,k}^T$, where $\mathbf{B}_{i,k}$ is the incidence block for agent i in the time-varying functional graph. It holds from the definition of the target configuration (2) that $\Theta^* = \mathbf{Z}_k^* \mathbf{B}_{i,k} \Phi_{i,k}^T$. We are now ready to rewrite (16) as follows

$$\psi_{i,k} = \frac{1}{N_{i,k}} \sum_{j \in \mathcal{N}_{i,k}} \left\| \hat{\Theta}_{i,k} - \hat{\Theta}_{j,k} \right\|_F^2 \quad (24a)$$

$$= \frac{1}{N_{i,k}} \sum_{j \in \mathcal{N}_{i,k}} \left\| (\hat{\Theta}_{i,k} - \Theta_k^*) - (\hat{\Theta}_{j,k} - \Theta_k^*) \right\|_F^2 \quad (24b)$$

$$= \frac{1}{N_{i,k}} \sum_{j \in \mathcal{N}_{i,k}} \left\| (\mathbf{Z}_k - \mathbf{Z}_k^*) (\mathbf{B}_{i,k} \Phi_{i,k}^T - \mathbf{B}_{j,k} \Phi_{j,k}^T) \right\|_F^2 \quad (24c)$$

$$\leq \frac{1}{N_{i,k}} \sum_{j \in \mathcal{N}_{i,k}} \left\| \mathbf{B}_{i,k} \Phi_{i,k}^T - \mathbf{B}_{j,k} \Phi_{j,k}^T \right\|_F^2 \left\| \mathbf{Z}_k - \mathbf{Z}_k^* \right\|_F^2 \quad (24d)$$

$$= \frac{N}{N_{i,k}} \sum_{j \in \mathcal{N}_{i,k}} \left\| \mathbf{B}_{i,k} \Phi_{i,k}^T - \mathbf{B}_{j,k} \Phi_{j,k}^T \right\|_F^2 \delta_k. \quad (24e)$$

■

B. Proof of Corollary 1

Proof. Recollect from the definition of CI (16) and use similar trick as in (24),

$$\psi_{i,k} = \frac{1}{N_{i,k}} \sum_{j \in \mathcal{N}_{i,k}} \left\| \hat{\boldsymbol{\Theta}}_{i,k} - \hat{\boldsymbol{\Theta}}_{j,k} \right\|_F^2 \quad (25a)$$

$$= \frac{1}{N_{i,k}} \sum_{j \in \mathcal{N}_{i,k}} \left\| (\hat{\boldsymbol{\Theta}}_{i,k} - \boldsymbol{\Theta}_k^*) - (\hat{\boldsymbol{\Theta}}_{j,k} - \boldsymbol{\Theta}_k^*) \right\|_F^2 \quad (25b)$$

$$= \frac{1}{N_{i,k}} \sum_{j \in \mathcal{N}_{i,k}} \left\| (\mathbf{Z}_k - \mathbf{Z}_k^*) (\mathbf{B}_{i,k} \boldsymbol{\Phi}_{i,k}^T - \mathbf{B}_{j,k} \boldsymbol{\Phi}_{j,k}^T) + (\mathbf{V}_{i,k} \boldsymbol{\Phi}_{i,k}^T - \mathbf{V}_{j,k} \boldsymbol{\Phi}_{j,k}^T) \right\|_F^2 \quad (25c)$$

$$= \psi'_{i,k} + \psi''_{i,k} + \psi'''_{i,k}, \quad (25d)$$

where the expressions for $\psi'_{i,k}$, $\psi''_{i,k}$ and $\psi'''_{i,k}$ are given in (26).

$$\psi'_{i,k} = \frac{1}{N_{i,k}} \sum_{j \in \mathcal{N}_{i,k}} \left\| (\mathbf{Z}_k - \mathbf{Z}_k^*) (\mathbf{B}_{i,k} \boldsymbol{\Phi}_{i,k}^T - \mathbf{B}_{j,k} \boldsymbol{\Phi}_{j,k}^T) \right\|_F^2 \quad (26a)$$

$$\psi''_{i,k} = \frac{1}{N_{i,k}} \sum_{j \in \mathcal{N}_{i,k}} \left\| (\mathbf{V}_{i,k} \boldsymbol{\Phi}_{i,k}^T - \mathbf{V}_{j,k} \boldsymbol{\Phi}_{j,k}^T) \right\|_F^2 \quad (26b)$$

$$\psi'''_{i,k} = \frac{2}{N_{i,k}} \sum_{j \in \mathcal{N}_{i,k}} \text{tr} \left[(\mathbf{B}_{i,k} \boldsymbol{\Phi}_{i,k}^T - \mathbf{B}_{j,k} \boldsymbol{\Phi}_{j,k}^T)^T (\mathbf{Z}_k \mathbf{Z}_k^*)^T (\mathbf{V}_{i,k} \boldsymbol{\Phi}_{i,k}^T - \mathbf{V}_{j,k} \boldsymbol{\Phi}_{j,k}^T) \right] \quad (26c)$$

We first define the expectation of the tracking error as

$$\mathbb{E}[\delta_k] = \frac{1}{N} \mathbb{E} \left[\left\| \mathbf{Z}_k - \mathbf{Z}_k^* \right\|_F^2 \right] \quad (27)$$

and the expectation of CI is

$$\mathbb{E}[\psi_{i,k}] = \mathbb{E}[\psi'_{i,k}] + \mathbb{E}[\psi''_{i,k}] + \mathbb{E}[\psi'''_{i,k}], \quad (28)$$

and we analyze each term individually. Since $\psi'_{i,k}$ is the same as (24c), we can directly rewrite

$$\mathbb{E}[\psi'_{i,k}] \leq \mathbb{E} \left[\frac{1}{N_{i,k}} \sum_{j \in \mathcal{N}_{i,k}} \left\| \mathbf{B}_{i,k} \boldsymbol{\Phi}_{i,k}^T - \mathbf{B}_{j,k} \boldsymbol{\Phi}_{j,k}^T \right\|_F^2 \left\| \mathbf{Z}_k - \mathbf{Z}_k^* \right\|_F^2 \right] \quad (29a)$$

$$= \frac{N}{N_{i,k}} \sum_{j \in \mathcal{N}_{i,k}} \left\| \mathbf{B}_{i,k} \boldsymbol{\Phi}_{i,k}^T - \mathbf{B}_{j,k} \boldsymbol{\Phi}_{j,k}^T \right\|_F^2 \mathbb{E}[\delta_k] \quad (29b)$$

For term $\psi''_{i,k}$ in (26),

$$\begin{aligned} \mathbb{E}[\psi''_{i,k}] &= \frac{1}{N_{i,k}} \sum_{j \in \mathcal{N}_{i,k}} \mathbb{E} \left[\left\| (\mathbf{V}_{i,k} \boldsymbol{\Phi}_{i,k}^T - \mathbf{V}_{j,k} \boldsymbol{\Phi}_{j,k}^T) \right\|_F^2 \right] \\ &= \frac{1}{N_{i,k}} \sum_{j \in \mathcal{N}_{i,k}} \mathbb{E} \left[\text{tr} [(\mathbf{V}_{i,k} \boldsymbol{\Phi}_{i,k}^T - \mathbf{V}_{j,k} \boldsymbol{\Phi}_{j,k}^T)^T (\mathbf{V}_{i,k} \boldsymbol{\Phi}_{i,k}^T - \mathbf{V}_{j,k} \boldsymbol{\Phi}_{j,k}^T)] \right] \end{aligned} \quad (30a)$$

$$\begin{aligned} &= \frac{1}{N_{i,k}} \sum_{j \in \mathcal{N}_{i,k}} \text{tr} [\boldsymbol{\Phi}_{i,k} \mathbb{E}[\mathbf{V}_{i,k}^T \mathbf{V}_{i,k}] \boldsymbol{\Phi}_{i,k}^T] \\ &\quad + \text{tr} [\boldsymbol{\Phi}_{j,k} \mathbb{E}[\mathbf{V}_{j,k}^T \mathbf{V}_{j,k}] \boldsymbol{\Phi}_{j,k}^T] \\ &\quad - 2 \text{tr} [\boldsymbol{\Phi}_{i,k} \mathbb{E}[\mathbf{V}_{i,k}^T \mathbf{V}_{j,k}] \boldsymbol{\Phi}_{j,k}^T] \end{aligned} \quad (30b)$$

$$\begin{aligned} &= \frac{1}{N_{i,k}} \sum_{j \in \mathcal{N}_{i,k}} \text{tr} [\mathbf{R}_{ij}] \text{tr} [\boldsymbol{\Phi}_{i,k} \boldsymbol{\Phi}_{i,k}^T] \\ &\quad + \text{tr} [\mathbf{R}_{ij}] \text{tr} [\boldsymbol{\Phi}_{j,k} \boldsymbol{\Phi}_{j,k}^T] + 0 \end{aligned} \quad (30c)$$

$$= \frac{\text{tr} [\mathbf{R}_{ij}]}{N_{i,k}} \sum_{j \in \mathcal{N}_{i,k}} \left\| \boldsymbol{\Phi}_{i,k} \right\|_F^2 + \left\| \boldsymbol{\Phi}_{j,k} \right\|_F^2, \quad (30d)$$

where we use Property 1 in Appendix B-C.

For term $\psi'''_{i,k}$ in (26),

$$\begin{aligned} \mathbb{E}[\psi'''_{i,k}] &= \mathbb{E} \left[\frac{1}{N_{i,k}} \sum_{j \in \mathcal{N}_{i,k}} \text{tr} [(\mathbf{B}_{i,k} \boldsymbol{\Phi}_{i,k}^T - \mathbf{B}_{j,k} \boldsymbol{\Phi}_{j,k}^T)^T (\mathbf{Z}_k - \mathbf{Z}_k^*)^T (\mathbf{V}_{i,k} \boldsymbol{\Phi}_{i,k}^T - \mathbf{V}_{j,k} \boldsymbol{\Phi}_{j,k}^T)] \right] \end{aligned} \quad (31a)$$

$$\begin{aligned} &= \frac{1}{N_{i,k}} \sum_{j \in \mathcal{N}_{i,k}} \text{tr} [(\mathbf{B}_{i,k} \boldsymbol{\Phi}_{i,k}^T - \mathbf{B}_{j,k} \boldsymbol{\Phi}_{j,k}^T)^T \\ &\quad \mathbb{E}[(\mathbf{Z}_k - \mathbf{Z}_k^*)^T (\mathbb{E}[\mathbf{V}_{i,k}] \boldsymbol{\Phi}_{i,k}^T - \mathbb{E}[\mathbf{V}_{j,k}] \boldsymbol{\Phi}_{j,k}^T)] \end{aligned} \quad (31b)$$

$$= 0, \quad (31c)$$

as the noises in matrices $\mathbf{V}_{i,k}$ for all i and k are zero-mean and not correlated with $\mathbf{Z}_k - \mathbf{Z}_k^*$.

From the expressions (29), (30) and (31), (28) is now in the form of

$$\mathbb{E}[\psi_{i,k}] \leq c_{i,k} \mathbb{E}[\delta_k] + b_{i,k}, \quad (32)$$

where

$$c_{i,k} = \frac{N}{N_{i,k}} \sum_{j \in \mathcal{N}_{i,k}} \left\| \mathbf{B}_{i,k} \boldsymbol{\Phi}_{i,k}^T - \mathbf{B}_{j,k} \boldsymbol{\Phi}_{j,k}^T \right\|_F^2, \quad (33)$$

and

$$b_{i,k} = \frac{\text{tr} [\mathbf{R}_{ij}]}{N_{i,k}} \sum_{j \in \mathcal{N}_{i,k}} \left\| \boldsymbol{\Phi}_{i,k} \right\|_F^2 + \left\| \boldsymbol{\Phi}_{j,k} \right\|_F^2. \quad (34)$$

■

C. Property

Property 1. Given a matrix $\mathbf{V} = [\mathbf{v}_1, \mathbf{v}_2, \dots, \mathbf{v}_N] \in \mathbb{R}^{D \times N}$ where $\mathbf{v}_i \stackrel{\text{i.i.d.}}{\sim} \mathcal{N}(\mathbf{0}_D, \mathbf{R})$, the following statement holds true

$$\mathbb{E}[\mathbf{V}^T \mathbf{V}] = \text{tr} [\mathbf{R}] \mathbf{I}_N. \quad (35)$$